JACS
JOURNAL OF THE AMERICAN CHEMICAL SOCIETY
Article
pubs.acs.org/JACS

# Extended-Charge-Transfer Excitons in Crystalline Supramolecular Photocatalytic Scaffolds

Nicholas J. Hestand,[†] Roman V. Kazantsev,[‡,§] Adam S. Weingarten,[‡,§] Liam C. Palmer,[‡,§,▽] Samuel I. Stupp,[*,‡,§,∥,⊥,#,▽] and Frank C. Spano[*,†]

[†]Department of Chemistry, Temple University, Philadelphia, Pennsylvania 19122, United States
[‡]Department of Chemistry, [§]Argonne—Northwestern Solar Energy Research (ANSER) Center, [∥]Department of Materials Science and Engineering, and [⊥]Department of Biomedical Engineering, Northwestern University, Evanston, Illinois 60208, United States
[#]Department of Medicine and [▽]Simpson Querrey Institute for BioNanotechnology, Northwestern University, Chicago, Illinois 60611, United States

Supporting Information

**ABSTRACT:** Coupling among chromophores in molecular assemblies is responsible for phenomena such as resonant energy transfer and intermolecular charge transfer. These processes are central to the fields of organic photovoltaics and photocatalysis, where it is necessary to funnel energy or charge to specific regions within the system. As such, a fundamental understanding of these transport processes is essential for developing new materials for photovoltaic and photocatalytic applications. Recently, photocatalytic systems based on photosensitizing perylene monomimide (PMI) chromophore amphiphiles were found to show variation in hydrogen gas ($H_2$) production as a function of nanostructure crystallinity. The 2D crystalline systems form in aqueous electrolyte solution, which provides a high dielectric environment where the Coulomb potential between charges is mitigated. This results in relatively weakly bound excitons that are ideal for reducing protons. In order to understand how variations in crystalline structure affect $H_2$ generation, two representative PMI systems are investigated theoretically using a modified Holstein Hamiltonian. The Hamiltonian includes both molecular Frenkel excitations (FE) and charge-transfer excitations (CTE) coupled nonadiabatically to local intramolecular vibrations. Signatures of FE/CTE mixing and the extent of electron/hole separation are identified in the optical absorption spectrum and are found to correlate strongly to the observed $H_2$ production rates. The absorption spectral signatures are found to sensitively depend on the relative phase between the electron and hole transfer integrals, as well as the diabatic energy difference between the Frenkel and CT exciton bands. Our analysis provides design rules for artificial photosynthetic systems based on organic chromophore arrays.

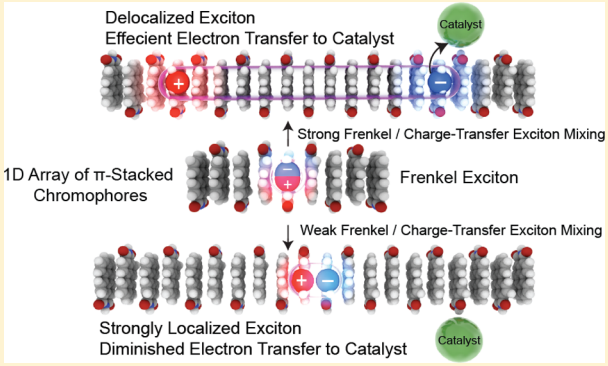


## I. INTRODUCTION

Natural photosynthetic systems organize chromophore molecules to absorb the sun's energy and efficiently transfer it to catalysts for solar-to-fuel conversion.[1,2] This energy flow ability relies on the precise chromophore−chromophore and chromophore−protein interactions that are afforded by the protein's tertiary supramolecular structure.[3] Emulation of such behavior in artificial systems has been a standing challenge for the last several decades. Over this time period, there have been great advances in the field of chromophore self-assembly into supramolecular arrays. Not only can nanostructure morphology be controlled through judicious molecular design,[4] but it is also well-established that chromophore arrays can facilitate many-body interactions, such as resonant energy transfer, making them attractive candidates for artificial photosynthesis.[5] However, the majority of photocatalysis investigations to date that involved organic chromophores were done with the molecules fully dissolved in solution.[6−8] In order to move forward with designing artificial systems based on chromophore arrays that can be considered photocatalytic materials, a detailed understanding of how intermolecular coupling modes and environmental effects impact their performance is required.

Recently some of us developed a supramolecular photocatalytic system based on the self-assembly of chromophore amphiphiles in water.[9] Constructed from a perylene monoimide (PMI) light-absorbing moiety covalently attached to a carboxylate headgroup (Figure 1a), these amphiphiles spontaneously self-assemble into ribbonlike structures that crystallize upon the addition of salt. The molecules within these structures are organized in a face-to-face manner, resulting in assemblies with a high degree of structural order. We found that

**Received:** June 2, 2016
**Published:** September 2, 2016



DOI: 10.1021/jacs.6b05673
J. Am. Chem. Soc. 2016, 138, 11762−11774

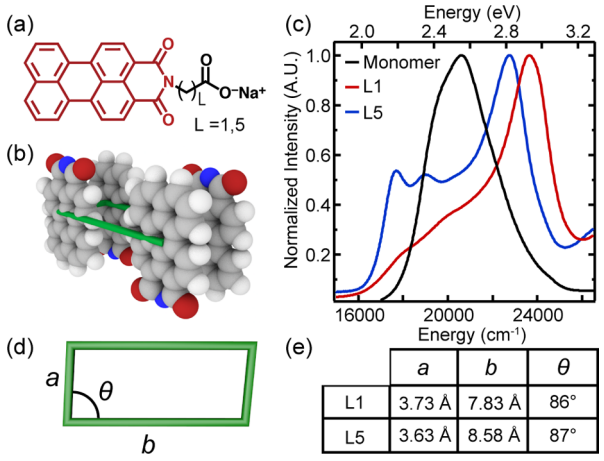


**Figure 1.** (a) Molecular structure of **L1** and **L5**. (b) Schematic showing antiparallel packing of **L1** and **L5** molecules within the supramolecular assembly. Imide side chains are omitted for clarity. (c) Normalized absorbance spectra of **L1** and **L5** in crystalline supramolecular nanostructures and as monomers. (d) Schematic of unit cell shown in part b. (e) Unit cell parameters for **L1** and **L5**.

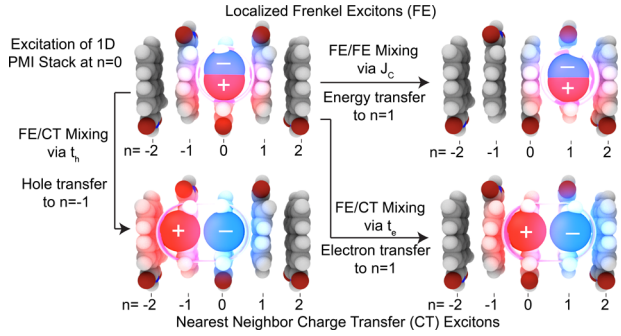


**Figure 2.** Graphical illustration of FEs and CTEs in PMI systems. A FE localized at $n = 0$ is shown in the top left corner. This FE can directly couple to a variety of FE and CTE states through the various matrix elements $J_c$, $t_e$, and $t_h$. For example, the exciton can transfer to site $n = 1$ via the long-range excitonic coupling $J_c$, as shown in the top right corner. The exciton can also dissociate via the charge transfer integrals $t_e$ and $t_h$. As shown in the lower left corner, $t_h$ facilitates hole transfer to a neighboring site while the electron remains at the parent molecule. The analogous processes for electron transfer is facilitated by $t_e$, as illustrated in the lower right corner. Note that the charge transfer process can repeat to yield larger-radius CTEs.

integrating these crystalline nanostructures with nickel-based proton reduction catalysts facilitated the photocatalytic production of hydrogen ($H_2$) gas. Interestingly, by modifying the alkyl spacer length between the chromophores and the solubilizing charge group of the molecule, we were able to alter the crystalline packing arrangement of the molecules within the nanostructures (Figure 1b,d,e).[10] This change in packing was accompanied by changes in intermolecular coupling among the chromophores, as evidenced by differences in the ground-state absorption spectra, including the energy of the absorption maximum and the energetic distribution of oscillator strength (Figure 1c). Importantly, we observed a discontinuous jump in the rate of $H_2$ evolution that directly correlated with a change in molecular crystal packing, in particular an increase in $b$ by about 1 Å in going from **L1** to **L5** (see Figure 1e).[10] Given that molecular packing has been shown to greatly impact device performance in organic photovoltaics,[11] we analyze here how intermolecular coupling in crystalline light-absorbing nanostructures affects the nature of their excited states and catalyst photosensitization abilities.

Our analysis is framed around the mixing between light-induced molecular (Frenkel) excitations, where the electron and hole reside on the same chromophore, and charge-transfer excitations (CTEs), where the electron and hole reside on different chromophores (see Figure 2). While the strongly dipole-allowed Frenkel excitations (FEs) are generally responsible for the majority of light absorption in molecular assemblies, CTEs can play a pivotal role in determining the optical and electronic properties of a supramolecular assembly.[12−25] Especially relevant to the current work, CTEs mediate the $H^+$ reduction reaction by facilitating electron transfer from the optically excited FE to the reducing nickel-based catalyst. Though CTEs absorb little light due to their inherently weak oscillator strength,[12,13] direct coupling to FEs results in nontrivial changes to the absorption and photoluminescence (PL) spectra. For instance, in the polyacene series, FE/CTE coupling plays a central role in determining the Davydov splitting and exciton dispersion,[14−19] while in the rylene family the same coupling can explain the absorption spectra of a variety of perylene and terrylene dyes.[12,13,20−25] Strong FE/CTE mixing also promotes excimer formation that results in broad, unstructured emission from many perylene assemblies.[26−28]

The significant FE/CTE mixing within many $\pi$-stacked molecular nanostructures requires models that include CTEs in order to satisfactorily describe the system photophysics.[12−15,20−25,29] In previous studies of $\pi$-stacked assemblies, the charge-transfer (CT) basis set was truncated to include only electron and hole pairs that lie on nearest neighbor molecules or within a short distance of one another.[12,14,15,20−23,25] Such truncations are justified considering that the large Coulomb binding energy of many organic molecular crystals (typically 0.2−0.4 eV) prohibits electron and hole separation much beyond nearest neighbors. If, however, the Coulomb potential is sufficiently screened (e.g., due to a high dielectric environment), the energies of larger-radius CTEs become comparable to those of the nearest-neighbor CTEs [see Figure S1, Supporting Information (SI)], resulting in significant mixing and extended electron−hole separation. For the subset of CT states that couple to the optically allowed FE, significant mixing among extended electron−hole CT states arises whenever $V_{CT}(1) \ll 4|t_e + t_h|$, where $V_{CT}(1)$ is the Coulomb binding energy for an electron and hole on neighboring sites (including screening) and $t_e$ and $t_h$ are the electron and hole transfer integrals. In other words, when the CT coupling among molecules (i.e., CTE bandwidth) greatly exceeds the Coulomb energy between electron and hole, the charges can separate easily into extended charge transfer excitons. Indeed, the PMI assemblies of interest here form in aqueous electrolyte solutions with large dielectric constants. As a result, we expect the effective (static) dielectric constant of these crystalline nanostructures to be much higher than those of bulk organic crystals, thereby necessitating extended CT states in a successful theoretical model.

In order to understand the photophysics of the PMI systems, we first investigate the role that CTEs play in the absorption spectral line shapes of $\pi$-stacked assemblies in high-dielectric environments. We identify spectral signatures of strong FE/CTE mixing involving states with large electron−hole separations. Such mixing is strong within PMI $\pi$-stacks where


DOI: 10.1021/jacs.6b05673
J. Am. Chem. Soc. 2016, 138, 11762−11774

the highest occupied and lowest unoccupied molecular orbitals (HOMO and LUMO, respectively) of adjacent PMI molecules interact strongly due to significant HOMO−HOMO and LUMO−LUMO wave function overlap. The magnitude and sign of these interactions are quantified by the electron ($t_e$) and hole ($t_h$) charge transfer integrals and sensitively depend on the nodal patterns of the relevant frontier molecular orbitals.[12,13,30−32] In our investigation, special attention is paid to the relative phase of $t_e$ and $t_h$, which determines the magnitude of FE/CTE mixing between states having the same symmetry.[12,13,20−25,33] In previous works, some of us showed that the relative phase between $t_e$ and $t_h$ has a strong impact on the absorption and emission spectral profiles and can tune the short-range CT-induced coupling between J- and H-aggregate behavior (as determined by the sign of the CT-induced coupling), even in the absence of the exciton (dipole−dipole) coupling.[22,23,34] This relative phase can further modulate the exciton mobility in tightly packed molecular $\pi$-stacks[32] and was recently shown to strongly impact electron/hole recombination rates.[35] Here, we are mainly concerned with how the relative phase between $t_e$ and $t_h$ affects charge separation to distant CT states. Finally, we apply the theory to two PMI systems, namely, PMI-L1 (**L1**) and PMI-L5 (**L5**), which were found experimentally to assemble into two distinct crystal-packing arrangements (Figure 1d,e).[10] By reproducing the absorption spectrum of both species, we provide a basis for understanding how intermolecular coupling affects their respective photosensitization abilities and observed photocatalytic properties. Specifically, we correlate the photosensitization ability of the two species, as quantified by the relative $H_2$ production rate when incorporated with a nickel-based proton reduction catalyst, to their absorption signatures.

## II. MODEL HAMILTONIAN

To model the optical and electronic properties of tightly packed molecular assemblies with weakly bound excitons, we utilize a Hamiltonian similar to that used in previous works[12,13,20−24] and employ a basis set that includes all CT states. Our Holstein-like Hamiltonian describes energy and charge transport in the presence of local vibronic coupling to the symmetric intramolecular mode (or cluster of modes) with energy $\omega_{vib} \approx 1400\ cm^{-1}$ ($\hbar = 1$), which is responsible for the vibronic progression observed in the solution spectra of PMI as well as in many other conjugated materials. The Hamiltonian, which assumes a single electron and a single hole, can be divided into Frenkel and CT components as

$$H = H_F + H_{CT} \tag{1}$$

The Frenkel Hamiltonian, including local vibronic coupling, is given by

$$H_F = -U\sum_n B_n^\dagger B_n + \sum_n \{J_c B_n^\dagger B_{n+1} + \text{H.c.}\} + \omega_{vib}\sum_n b_n^\dagger b_n + \omega_{vib}\sum_n \{\lambda_0(b_n^\dagger + b_n) + {\lambda_0}^2\} B_n^\dagger B_n \tag{2}$$

and describes energy transfer across a linear one-dimensional $\pi$-stack of PMI chromophores. In eq 2 the zero of energy is chosen to correspond to the infinitely separated electron and hole. The operator $B_n^\dagger$ ($B_n$) creates (annihilates) a local Frenkel excitation on the $n$th chromophore with local electrostatic binding energy $U$, while direct energy transfer between nearest neighbor chromophores occurs via Coulombic excitonic coupling, as quantified by $J_c$ (see Figure 2). Such coupling is normally understood to arise from the interaction between molecular transition dipoles.[36−38] A Frenkel excitation consists of an electron and hole occupying the same molecular site, and hence, $B_n^\dagger = c_n^\dagger d_n^\dagger$, where $c_n^\dagger$ ($d_n^\dagger$) creates an electron (hole) on molecule $n$. The operator $b_n^\dagger$ ($b_n$) creates (annihilates) a vibrational excitation on molecule $n$, and the vibrational coupling to the Frenkel excitation is determined by the neutral Huang−Rhys (HR) parameter ${\lambda_0}^2$.

The CT Hamiltonian describes charge transfer across the $\pi$-stack and is written as

$$H_{CT} = \sum_n \{t_e c_n^\dagger c_{n+1} + t_h d_n^\dagger d_{n+1} + \text{H.c.}\} - \sum_{n,s\neq 0} V_{CT}(s) c_n^\dagger c_n d_{n+s}^\dagger d_{n+s} + \omega_{vib}\sum_{n,s\neq 0} \{\lambda_-(b_n^\dagger + b_n) + \lambda_+(b_{n+s}^\dagger + b_{n+s}) + {\lambda_-}^2 + {\lambda_+}^2\} \times c_n^\dagger c_n d_{n+s}^\dagger d_{n+s} \tag{3}$$

The electron and hole transfer integrals, $t_e$ and $t_h$, facilitate charge migration throughout the system by coupling nearest neighbor HOMOs and LUMOs, respectively (see Figure 2), while vibronic coupling to the CT states is described by the ionic HR factors ${\lambda_+}^2$ (for holes) and ${\lambda_-}^2$ (for electrons). The Coulombic binding energy for an electron−hole pair separated by $|s|d$, where $d$ is the distance between nearest neighbor chromophores, is given by $V_{CT}(s) = e^2/4\pi\varepsilon_0\varepsilon_r|s|d$, where $\varepsilon_r$ is the effective static dielectric constant of the system plus environment. The first term in eq 3 also accounts for FE/CTE mixing through exciton dissociation and recombination. The dissociation integrals ($D_e$ and $D_h$) describing these processes have been approximated by their one-electron components, $t_e$ and $t_h$.[39]

The Hamiltonian in eq 1 is readily expressed in a multiparticle basis set consisting of one-, two-, and three-particle FE states and two- and three-particle CTE states, as described in greater detail in the Supporting Information and in previous publications.[40−43] In the current work, all charge-separated states are retained in the basis set, regardless of the distance between electron and hole. While the two-particle approximation[40−42] is generally appropriate, we found that inclusion of both Frenkel and CT three-particle states is necessary to achieve sufficient convergence for the PMI assemblies due to their large CT integrals and the near resonance condition between the diabatic CT and Frenkel states. However, in order to reduce the basis set to a manageable size, the three-particle Frenkel and CT states have been truncated so that the pure vibrational excitations remain within a two-molecule radius of the vibronic excitation. This truncation results in a dramatic increase in computational efficiency without sacrificing accuracy. In addition, we assume periodic boundary conditions in order to exploit system symmetries to reduce computation time.

In a periodic system where translational symmetry applies (i.e., crystalline solid), each eigenstate is characterized by a wave vector $k = 0, \pm 2\pi/N, \pm 4\pi/N, \ldots, \pi$., which is a good quantum number of the state. Accordingly, we express the diabatic Frenkel states as


DOI: 10.1021/jacs.6b05673
J. Am. Chem. Soc. 2016, 138, 11762−11774

$$|k\rangle = \frac{1}{\sqrt{N}} \sum_n e^{ikn} |n\rangle \tag{4}$$

where $|n\rangle$ represents a local FE on molecule $n$. The diabatic CT states are labeled with wave vector $k$ and the separation between electron and hole, $s$,

$$|k, s\rangle = \frac{1}{\sqrt{N}} \sum_n e^{ikn} |n, n+s\rangle \tag{5}$$

where $|n, n+s\rangle$ represents the local state having a hole on molecule $n$ and an electron on molecule $n+s$ ($s = 1, 2, ..., N-1$). In the basis defined by eqs 4 and 5, the Hamiltonian couples electronic excitations with like values of $k$,[12,24,25,33]

$$\langle k|H|k\rangle = (J_k - U) \tag{6}$$

$$\langle k, s|H|k, s'\rangle = (t_e + t_h e^{\mp ik}) \delta_{s,s'\pm 1} \tag{7}$$

$$\langle k|H|k, s\rangle = (t_e + t_h e^{\mp ik}) \delta_{s,\pm 1} \tag{8}$$

where the exciton coupling term is defined by $J_k = 2J_c \cos(k)$. The electronic states are written in this manner and then dressed with vibrations (see the SI) in order to form a multiparticle basis set in which $k$ remains a good quantum number. The Hamiltonian is divided into sub-blocks according to $k$ and each sub-block is numerically diagonalized to yield all eigenstates and eigenvalues associated with the wave vector. Once the eigenstates and eigenvalues are known, the observables are calculated (see the SI for calculation details).

In order to gain insight into the underlying physics of extended CT states and specifically their impact on the photophysics and photosensitization ability of PMI assemblies, we consider a simplified model valid in the limit of strongly screened Coulombic interactions, $V_{CT}(1) \ll 4|t_e + t_h|$, which, as we show below, is valid for the PMI systems of interest. We therefore begin our analysis by taking $V_{CT}(s) = 0$ in eq 3 and neglecting (for now) vibrational coupling ($\lambda_0^2 = \lambda_+^2 = \lambda_-^2 = 0$). The solution to a slightly more complex model for an infinite 1D system where $V_{CT}(s) \neq 0$ was given by Merrifield.[33] Under our assumptions, the subspaces composed of Frenkel and CT states can be diagonalized analytically, leaving only the coupling between the Frenkel and CT states to contend with. Subspace diagonalization results in the Frenkel states according to eq 4 and the CT states defined by

$$|k, p\rangle = \sqrt{\frac{2}{N}} \sum_s e^{i\theta(k)s} \sin(ps) |k, s\rangle \tag{9}$$

where we have introduced $p = \pi/N, 2\pi/N, ..., (N-1)\pi/N$ as the quasirelative momentum between electron and hole, and the exponential phase factor $\theta(k) = 2\,\mathrm{atan}[\mathrm{Im}[z]/(|z| + \mathrm{Re}[z])$ for $k \neq \pi$ and $\theta(k) = \pi$ for $k = \pi$ where $z = t_e + t_h e^{ik}$. Throughout the remainder of the paper, we refer to the electronic basis defined by eqs 4 and 9 as the diabatic $k,p$-basis.

With the CT states expressed in this manner, the Hamiltonian matrix elements between electronic excitations are given by eq 6 along with[33]

$$\langle k, p|H|k, p\rangle = 2|t_e + t_h e^{ik}| \cos(p) \tag{10}$$

and

$$\langle k|H|k, p\rangle = \sqrt{\frac{2}{N}} (t_e + t_h e^{-ik}) e^{i\theta(k)} \sin(p) + \sqrt{\frac{2}{N}} (t_e + t_h e^{ik}) e^{i\theta(k)(N-1)} \sin(p(N-1)) \tag{11}$$

For systems in which all chromophores have parallel transition dipole moments, only states with wave vector $k = 0$ absorb visible radiation. In this important case, the relevant FE/CTE coupling is

$$\langle k = 0|H|k = 0, p\rangle = \sqrt{8/N} (t_e + t_h) \sin(p) \tag{12}$$

for $p = \pi/N, 3\pi/N, ...$ and is equal to zero when $p$ is an even multiple of $\pi/N$. Note that in the diabatic $k,p$-basis, the energies of the CT basis states (eq 10), along with the magnitude of the FE/CTE coupling (eq 11), depend on the relative phases of $t_e$ and $t_h$. As noted previously,[12,13,30−32] the CT integrals are very sensitive to the nanostructure packing geometry, since they depend on the overlap of the molecular HOMOs and LUMOs; this is especially well-known in the field of crystallochromy, where variations in crystal packing result in significant changes of the crystal color.[44−50] Because of this sensitivity, it has been suggested that modifying the packing structure (e.g., via chemical tuning[51−54]) may provide a useful route toward designing materials for organic electronics. The Hamiltonian expressed in the $k,p$-basis (eqs 6,10, and 11) serves as a launching point for our investigations of FE/CTE mixing in the sections that follow.

## III. ABSORPTION SIGNATURES OF FE/CTE MIXING

In this section we analyze the absorption spectral profile for $\pi$-stacked assemblies using the Hamiltonian in eq 1 in the high dielectric limit, $V_{CT}(1) \ll 4|t_e + t_h|$. Prior to irradiation with light, the $\pi$-stack is in the vibrationless electronic ground state $|G\rangle$ with energy $E_g$. Optical excitation induces transitions from $|G\rangle$ to the mixed FE/CTE eigenstates $|k, \alpha\rangle$ of eq 1 with energies $E_{k,\alpha}$ where $\alpha = 1, 2, ...$ in order of increasing energy. The transitions, which occur at energies $E_{k,\alpha} - E_g$, are governed by the oscillator strengths, which scale with the square of the transition dipole moment $|\langle G|\hat{\boldsymbol{\mu}}|k, \alpha\rangle|^2$. Here, $\hat{\boldsymbol{\mu}} \equiv \boldsymbol{\mu} \sum_n (B_n^\dagger + B_n)$ is the transition dipole moment operator. In this section, our primary goal is to identify signatures in the absorption spectrum that might provide clues to efficient electron/hole separation and therefore the catalytic efficiency of proton reduction systems where PMI nanostructures are used as the photosensitizing agent.

In the discussion that follows, we assume parallel transition dipole moments $\boldsymbol{\mu}$ for all chromophores within a disorder-free $\pi$-stack with a length much shorter than an optical wavelength. Under these conditions, oscillator strength is concentrated in the $k = 0$ FE in eq 4. The oscillator strengths to the mixed FE/CTE eigenstates, $|k, \alpha\rangle$, are therefore governed by

$$|\langle G|\hat{\boldsymbol{\mu}}|k, \alpha\rangle|^2 = N\boldsymbol{\mu}^2 |\langle k|k, \alpha\rangle|^2 \delta_{k=0} \tag{13}$$

where we have neglected the very weak oscillator strengths associated with the $(k = 0, p)$ CT states in eq 9.[12,13] Mixing of the $k = 0$ CTE states in eq 12 with the $k = 0$ FE (referred to from here on simply as the FE and CTE states) results in a distribution of oscillator strength over a broad range of mixed FE/CTE states. Figure 3 illustrates how such FE/CTE mixing depends on the system parameters $t_e$, $t_h$, $J_k$, and $U$, where we have taken $V_{CT}(s) = 0$ to reflect the high dielectric medium and


DOI: 10.1021/jacs.6b05673
J. Am. Chem. Soc. 2016, 138, 11762−11774

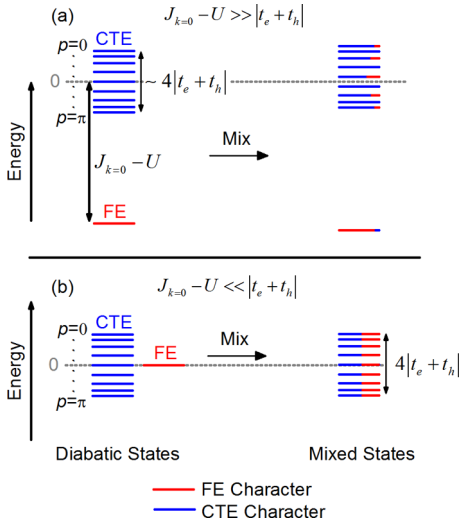


**Figure 3.** Qualitative energy level diagrams illustrating mixing between $k = 0$ FE and CT states in the weak (a) and strong (b) coupling regimes. The FE character of the eigenstates, $|\langle k = 0|k = 0, \alpha\rangle|^2$, is represented in red and the CTE character is represented in blue. The diabatic states (before mixing) are shown on the left, while the mixed states are shown on the right.

have temporarily ignored vibronic coupling. The quantity $|J_{k=0} - U|$ determines the energy separation between the FE and the CT band of states, while the sum $|t_e + t_h|$ serves to determine both the magnitude of the FE/CTE coupling as well as the CTE bandwidth for states with $k = 0$ (see eq 10).[12,13,20,25,33]

When $|J_{k=0} - U| \gg |t_e + t_h|$ (Figure 3a), the diabatic FE and CTE bands are energetically well separated, limiting the FE/CTE mixing. In this regime, FE/CTE mixing is dominated by the first-order processes described by eq 12; only CT states characterized by $p = \pi/N, 3\pi/N, \ldots$ appreciably mix with the FE, as very little second-order mixing between CT states occurs via indirect coupling through the FE state. This results in an uneven distribution of FE character across the mixed FE/CTE states with the majority of FE character being retained by the parent FE state. In this limit, the CTE states remain mostly inaccessible by optical excitation and therefore do not play a major role in the photophysical response of the assembly. The small degree of FE character that does mix into these states (shown in Figure 3a) scales as a sinusoidal function of $p$ (see eq 12). Furthermore, the mixed states exhibit a small energetic shift compared to the parent states due to the FE/CTE coupling as the FE and CTE states split away from one another.

In the opposite limit of $|J_{k=0} - U| \ll |t_e + t_h|$ (Figure 3b), the FE/CTE states are energetically well positioned for strong mixing to occur. The diabatic CT states interact strongly with one another via indirect coupling through the diabatic FE. Indeed, in the limit $J_{k=0} - U = 0$ it can be shown that the FE character is distributed evenly across all $N$ mixed states. In this limit, the FE character per unit frequency interval scales directly with the density of states. Here the CTE states are optically accessible and play a much larger role in the assembly's photophysics.

The two limits of FE/CTE coupling are characterized by very different absorption spectral line shapes. Figure 4 illustrates how the spectrum changes as the ratio $M = (J_{k=0} - U)/|t_e + t_h|$ is varied for a system of chromophores arranged in a 1D linear

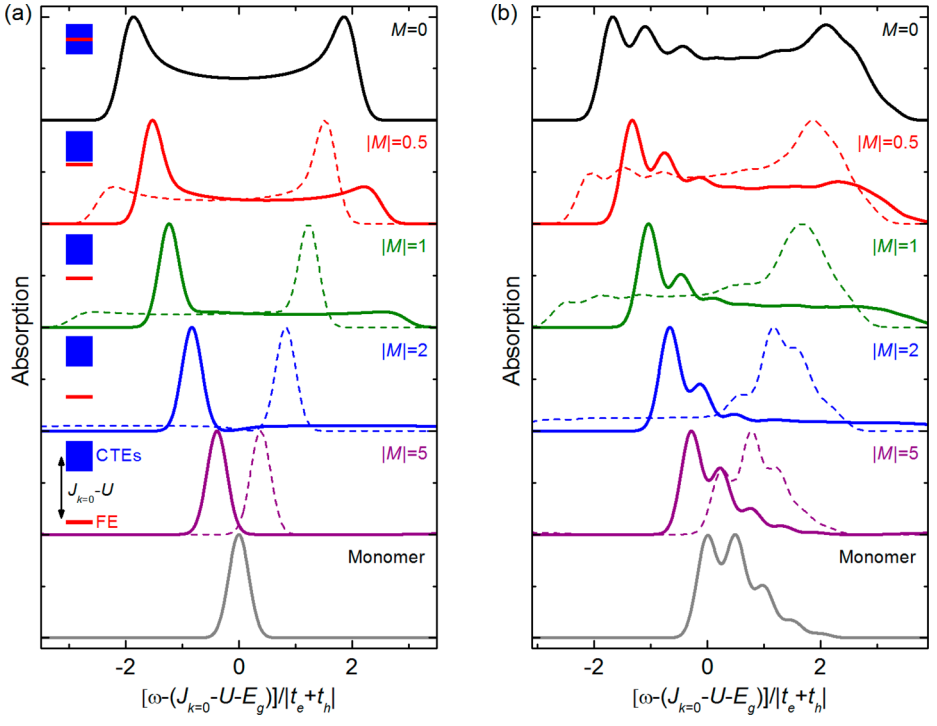


**Figure 4.** Simulated absorption spectra for (a) rigid and (b) nonrigid systems with various strengths of FE/CTE mixing as determined by the ratio $M = (J_{k=0} - U)/|t_e + t_h|$. For solid curves, $M$ is negative, placing the diabatic CT band above the FE, while in the dashed curves, $M$ is positive, so that the CT band lies below the FE. The inset in part (a) represents the relative energy of the FE and CT states for negative values of $M$. For all simulations $t_e = t_h$ and $V_{CT} = 0$. Additionally, for (b) we have set $J_{k=0}$ (in order to isolate the effects of FE/CTE mixing), and have taken $\omega_{vib} = (t_e + t_h)/2$ and $\lambda_0^2 = 2\lambda_+^2 = 2\lambda_-^2 = 1$.



DOI: 10.1021/jacs.6b05673
J. Am. Chem. Soc. 2016, 138, 11762−11774

$\pi$-stack. For simplicity we set $t_e = t_h$. In addition, we temporarily neglect the frequency dependence of the oscillator strength in order to better appreciate the band symmetries. Figure 4a contains simulations of rigid systems, while Figure 4b contains the corresponding simulations when vibronic coupling is activated.

We begin by discussing the absorption signatures in the absence of vibronic coupling. When $M$ is large and negative (Figure 4a, solid purple curve), the FE/CTE mixing is limited due to the large energy difference between Frenkel and CT states (see Figure 3a). The majority of oscillator strength resides in the transition to the lowest-energy exciton, which is composed of mostly FE character, and the absorption spectrum exhibits a single peak, red-shifted from the monomer absorption peak (Figure 4a, solid gray curve). Note that this red shift is due entirely to FE/CTE mixing. As $M$ increases toward zero (Figure 4a, solid blue, green, and red curves), the FE/CTE mixing is enhanced, resulting in the appearance of a weak but broad absorption band that is blue-shifted from the monomer absorption peak. The eigenstates responsible for the broad, high-energy band have dominant CT character and are made optically accessible by their small but non-negligible FE component. When $M = 0$ (Figure 4a, black curve) the broad band becomes far more intense and is dispersed symmetrically around the diabatic FE state (see eqs 6 and 10 and Figure 1b). The band, centered about $\omega = J_{k=0} - U - E_g$, has a width given by $4|t_e + t_h|$ (see Figure 5a, top). As $M$ is further increased above zero so that the FE lies *above* the CT band (the dashed curves in Figure 4a), the asymmetry of the spectrum reverses: the blue-shifted band retains the majority of the oscillator strength due to its dominant FE character, while the red-shifted band absorbs weakly due to its dominant CT character.

When vibronic coupling is included, the spectra exhibit nearly the same spectral signatures of FE/CTE mixing as the rigid systems (see Figure 4b). The asymmetry of the absorption line shape is still determined by the relative energy of the Frenkel and CT excitons, even though they are now dressed with vibrations. When the FE lies below the CTE band (Figure 4b, solid curves), the absorption spectrum is skewed to the red. On the other hand, when the FE lies above the CTE band (Figure 4b, dashed curves), the absorption spectrum is skewed to the blue. Most importantly, when the FE is near resonance with the CTE band ($|J_{k=0} - U| \ll |t_e + t_h|$), the bandwidth remains approximately equal to $4|t_e + t_h|$ and therefore persists as an accurate measure of the sum of the CT integrals. Finally, we note that for the simulations including vibronic coupling we have set $\omega_{vib} = |t_e + t_h|/2$, so that both the red- and blue-shifted bands due to FE/CTE mixing are clearly observable. For systems characterized by $\omega_{vib} \gg |t_e + t_h|$, the signatures of FE/CTE mixing will be largely masked by the vibronic progression.

The intensity and oscillator strength distribution of the spectral bands in Figure 4 can be used as a diagnostic tool to investigate what molecular states are involved during light absorption. The intensity of the broad band in Figure 4, reflects the coupling between the diabatic Frenkel state with CT states of extended electron–hole separation: restricting the coupling to only nearest neighbor CT states results in two distinct bands, separated by $2\sqrt{2}|t_e + t_h|$, with minimal intensity in the spectral region between the two peaks.[23] This behavior is emphasized in Figure 5 for the case $M = 0$ for both rigid (Figure 5 upper) and nonrigid (Figure 5, lower) $\pi$-stacks. When the FE state is allowed to mix only with nearest-neighbor CTEs (Figure 5, gray dashed curve), there is virtually no oscillator strength in the spectral region between the two main absorption bands. By contrast, when the Coulomb binding energy is severely compromised due to a high dielectric environment (Figure 5, solid black curve), the electron and hole can achieve maximal separation, leading to significant intensity between the two peaks (and an increased splitting to $4|t_e + t_h|$). The origin of this new intensity can be rationalized by examining the density of states for both the nearest-neighbor and extended CT cases (Figure 5, parts b and c, respectively). Mixing of the FE with only nearest-neighbor CTEs results in two energetically discrete optically active states. For the extended CT case, mixing the FE with $n - 1$ CTEs ($k = 0, p$) creates a band of optically active

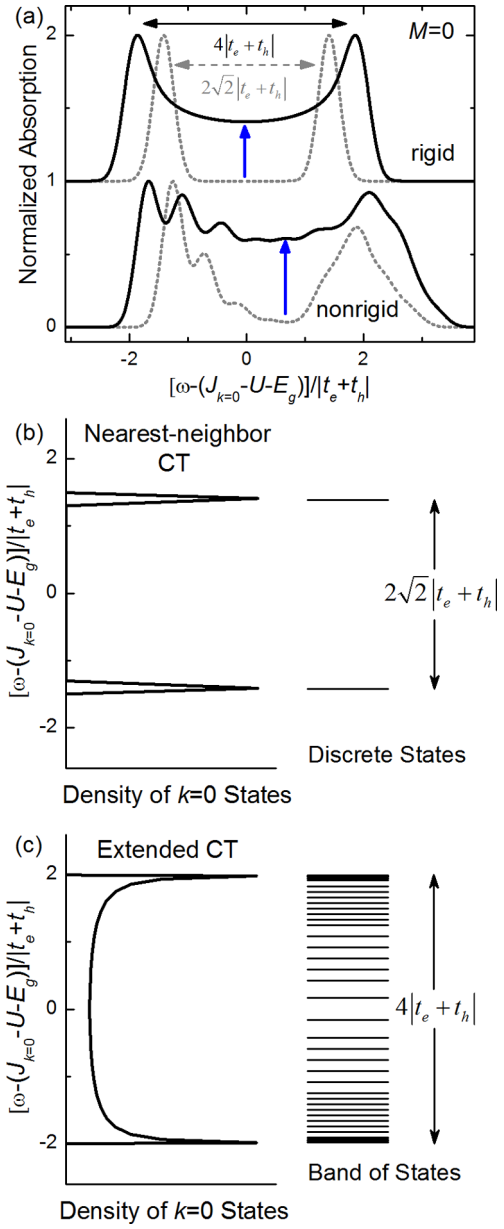


**Figure 5.** (a) Absorption spectra of rigid (upper) and nonrigid (lower) systems when the electron and hole are either restricted to nearest neighbors (gray dash) or allowed to separate to infinity (solid black). In all cases, $M = (J_{k=0} - U)/|t_e + t_h| = 0$ and $t_e = t_h$, while for the simulations accounting for vibronic coupling we have set $\lambda_0^2 = 2\lambda_+^2 = 2\lambda_-^2 = 1$ and $\omega_{vib} = (t_e + t_h)/2$. The blue arrows indicate the increase in absorption intensity due to the weakened Coulomb binding energy. (b, c) The density of states associated with the rigid spectra.



DOI: 10.1021/jacs.6b05673
J. Am. Chem. Soc. 2016, 138, 11762–11774

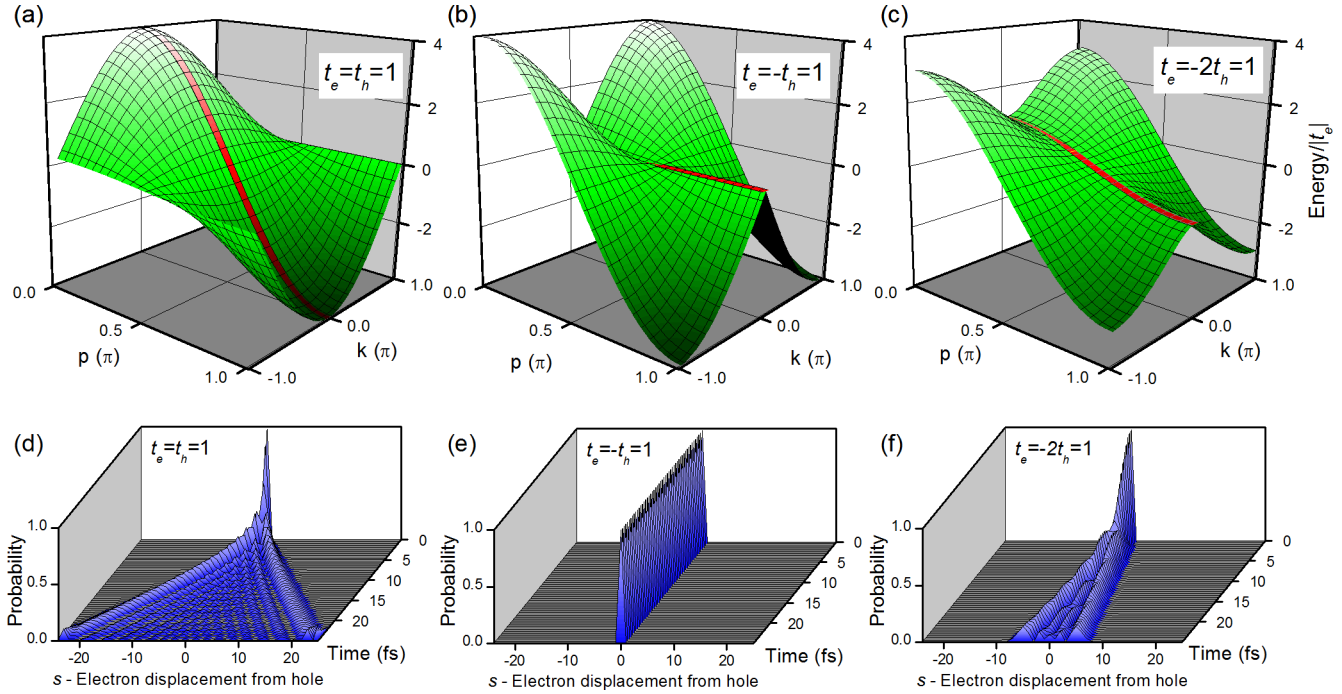


**Figure 6.** (a–c) The dispersion curves of CT basis states in the diabatic $k,p$-basis (eq 10) as a function of $k$ and $p$ for several relative phases of the CT integrals. The dispersion of CT states at $k = 0$ is highlighted in red. (d–f) The probability of being in the CT state $|k = 0, s\rangle$ at time $t$ after the system is initially placed in the $|k = 0\rangle$ Frenkel state. Parts d–f correspond to the dispersion curves in parts a–c. For all calculations $\lambda_0^2 = \lambda_+^2 = \lambda_-^2 = 0$, $J_k = 0$, $N = 50$, and the CT integrals indicated in the figure in units of vibrational quanta $\omega_{vib} = 1400$ cm$^{-1}$.

states. The majority of these states will be near the band edges, but some will lie in the center of the band. Hence, the interband absorption intensity serves as a signature for the presence of optically accessible CT states with substantial electron/hole separation.

The above analysis shows that when $|t_e + t_h| \gg |J_{k=0} - U|$ CT states are efficiently generated in $\pi$-stacked assemblies via optical absorption, underscoring the importance of the relative phase between $t_e$ and $t_h$ in determining FE/CTE mixing.[12,13,20−25,33] Importantly, a positive constructive interference between $t_e$ and $t_h$ not only enhances FE/CTE mixing, but also allows for the efficient optical generation of $k = 0$ CT states with electron/hole separation far beyond nearest neighbors. The latter occurs whenever $4|t_e + t_h| \gg V_{CT}(1)$, which is easy to satisfy in an environment with a high dielectric constant.

## IV. CHARGE SEPARATION DYNAMICS

In order for peryelene-based $\pi$-stacks to act as efficient scaffolds for photocatalysis, they must be able to rapidly supply electrons to the sites where catalytic reduction occurs. In order to appreciate the rate of electron production through exciton dissociation, and how such a rate is related to certain signatures in the absorption spectrum, we study in this section the dynamics of charge separation. Equations 7, 8, and 10 predict that the rate at which electrons and holes separate is a strong function of the CT bandwidth. Equations 7 and 8 show that for a given wave vector, charge separation is governed by $|t_e + t_h e^{ik}|$, while eq 10 shows that the CT bandwidth (for a given $k$) is proportional to the same term. For states relevant to optical absorption ($k = 0$), the ability of the charges to separate depends on the sum $|t_e + t_h|$. A large absorption bandwidth therefore signifies rapid charge separation (see section III).

Figure 6a–c illustrates the dispersion of the diabatic CT states as a function of $k$ and $p$ for systems characterized by CT integrals of different relative phases. When the CT integrals are in phase (Figure 6a), the $k = 0$ CT band (highlighted in red) has a large bandwidth, supporting rapid charge separation. On the other hand, when the CT integrals are individually small or out-of-phase (Figures 6b,c), the $k = 0$ CT bandwidth is small, suggesting suppressed charge separation.

In order to visualize the time-dependent evolution of charge separation as a function of CT coupling in our systems, we solved the time-dependent Schrödinger equation after initially exciting the system to the superposition state defined by

$$|\Psi(t=0)\rangle = \sum_i c_i |\Psi_i\rangle \tag{14}$$

$$c_i = \frac{1}{\boldsymbol{\mu}\sqrt{N}} \langle G|\hat{\boldsymbol{\mu}}|\Psi_i\rangle \tag{15}$$

In effect, $|\Psi(t=0)\rangle$ mimics the state of the system directly after broadband absorption. After excitation, the system is allowed to propagate coherently while the charge separation is monitored. We note that the state $|\Psi(t=0)\rangle$ is composed entirely of $k = 0$ FEs, so that at $t = 0$, there is no charge separation. The dependence of the charge separation behavior on the $|k = 0, p\rangle$ dispersion (i.e., CT bandwidth) is illustrated in Figure 6d–f, where the $|k = 0, s\rangle$ admixture of $|\Psi(t)\rangle$ is plotted as a function of time. Indeed, when $t_e$ and $t_h$ are in phase, as in Figure 6a, we observe efficient charge separation, as indicated by the rapid increase in $|k = 0, s \neq 0\rangle$ character of $|\Psi(t)\rangle$ with time (Figure 6d). The charges separate nearly 40 molecules away from one another after 25 fs. In sharp contrast, when $t_e$ and $t_h$ are out-of-phase, as in Figure 6b, the charges remain together indefinitely; the molecules do not couple via charge transfer, preventing $|\Psi(t)\rangle$ from evolving into a mixed FE/CTE state (Figure 6d). In the intermediate coupling case (Figure 6f), the charges separate but do not achieve as large of a spatial


DOI: 10.1021/jacs.6b05673
J. Am. Chem. Soc. 2016, 138, 11762−11774

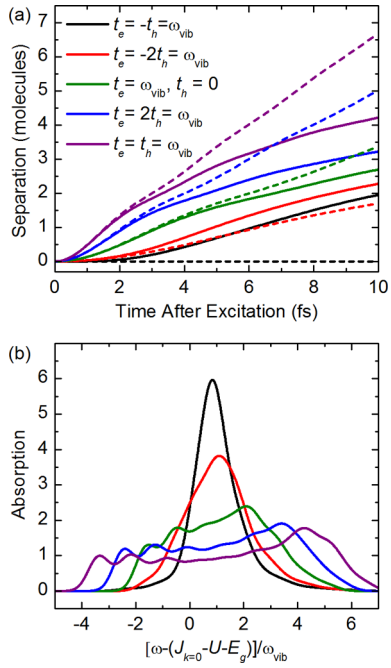


**Figure 7.** (a) The average CT separation as a function of time after excitation to $|\Psi(t=0)\rangle$ with (solid curves) and without (dashed curves) vibronic coupling. For these simulations, $J_k = 0$, $V_{CT} = 0$, $U = 0$, and $\omega_{vib} = 1400\ cm^{-1}$. For the simulations including vibronic coupling we have set $\lambda_0^2 = 2\lambda_+^2 = 2\lambda_-^2 = 1$, while all HR factors are set to zero when vibronic coupling is neglected. (b) The corresponding absorption spectra, including vibronic coupling. In all cases the simulations consider linear 1D chains of 50 chromophores.

separation as when the CT integrals are fully in-phase. This data indicates that the rate of charge separation scales directly with the $k = 0$, $p$ CT bandwidth.

A more quantitative measure of the charge separation dynamics is shown in Figure 7a. Here, the average electron/hole separation as a function of time is shown for several systems characterized by different CT integrals. The dotted lines represent the solution to the time-dependent Schrödinger equation in the absence of vibrational coupling ($\lambda_0^2 = \lambda_+^2 = \lambda_-^2 = 0$), and the solid lines are the solution when vibrational coupling is included. The corresponding absorption spectra for the simulations including vibrational coupling are shown in Figure 7b. In all cases, we have assumed that the diabatic Frenkel exciton lies in the middle of the CT band (see Figure 3b) by setting $J_k = U = V_{CT} = 0$. This resonance condition ensures an upper limit to the rate of charge separation for a given set of CT integrals and Huang–Rhys parameters. As the quantity $|J_{k=0} - U|$ increases, the rate of charge separation is expected to decrease as the FE and CTE states move away from resonance. Figure 7a shows that the rate of charge separation is directly correlated to the sum $|t_e + t_h|$; when the sum is small, the charge separation is slow, and as the sum increases, the rate of charge separation also increases. This result is in agreement with recent theoretical research, where it was shown that *minimizing* $|t_e + t_h|$ suppresses the rate of charge recombination at bulk heterojunction interfaces.[35] When including vibrational coupling, the electron and hole separate twice as fast when $t_e = t_h$ compared to the case of $t_e = -t_h$. This suggests that optimizing materials to have large, in-phase CT integrals would benefit applications that rely on efficient charge separation after absorption, such as organic photovoltaics and photocatalytic sensitizing agents.

Interestingly, in the absence of vibrational coupling, the charges remain bound to the same molecule when $t_e = -t_h$, as predicted by eqs 10 and 11. However, vibronic coupling allows the charges to separate at a rate that is only several times smaller than the maximal rate obtained when $t_e$ and $t_h$ are in phase (see black curve in Figure 7a). This is quite a nonintuitive result, since vibronic coupling generally increases the effective mass of the charges (i.e., slows them down). We interpret that vibronic coupling acts to interrupt the destructive interference resulting when $t_e$ and $t_h$ are perfectly out-of-phase, thereby allowing charges to separate.

The charge separation behaviors depicted in Figure 7a can be anticipated by certain spectral signatures present in the absorption spectrum, as demonstrated in Figure 7b. Systems exhibiting the fastest charge separation rates are characterized by a large absorption bandwidth, i.e., large in-phase CT integrals (see section III). On the other hand, slow charge separation is associated with a narrow absorption profile, signifying individually small or out-of-phase CT integrals. We again emphasize the importance of extended CT states being energetically accessible to the FE in order for good charge separation to occur. Otherwise, the electron and hole remain bound within a small radius exciton. As discussed in section III, the coupling to extended CT states is signified by enhanced oscillator strength between the two absorption bands (see Figure 5).

## V. APPLICATION TO PHOTOCATALYSIS WITH PERYLENE MONOIMIDE ASSEMBLIES

We now apply our theory to two photosensitizing PMI systems, PMI-L1 (**L1**) and PMI-L5 (**L5**) (Figure 1a). Dissolution of these molecules in water produces micron-long 1D ribbon structures driven by hydrophobic collapse of the aromatic portion of the molecule. Under charge-screening conditions, the molecules within these supramolecular assemblies crystallize, forming solution-dispersed 2D organic crystals. Both **L1** and **L5** organize into similar unit cells composed of antiparallel-oriented molecules (Figure 1b). However, analysis of the X-ray patterns shows slight differences in the crystalline packing arrangement (Figure 1d,e).[55] Furthermore, despite having identical *monomer* absorption profiles, these two crystals show significant differences in both the blue and red portion of the absorption spectra (Figure 1c). **L1** exhibits a blue-shifted main absorption peak along with a pronounced reduction in oscillator strength in the red region of the spectrum compared to **L5**. When interfaced with the same nickel-based proton reduction catalyst[10] under identical experimental conditions, assemblies containing **L5** evolve 2.4 ± 0.5 times more $H_2$ than those containing **L1**. We note that in the photocatalytic assemblies, the function of the PMI chromophores is to act as a photosensitizing agent (see ref 9). As the $H^+$ reduction catalyst is expected to behave similarly in both systems, the difference in $H_2$ production can be attributed to the ability of the PMI chromophores to generate and deliver electrons to the catalytic sites. Information about these processes can be uncovered by employing the correlations between absorption spectral signatures and FE/CTE mixing developed in sections II–IV.

Both **L1** and **L5** exhibit broad absorption spectra that are skewed to the blue, somewhat reminiscent of the dashed spectra in Figure 4b when $M$ is near zero. The spectral profiles indicate strong $k = 0$ FE/CTE mixing through in-phase CT


DOI: 10.1021/jacs.6b05673
J. Am. Chem. Soc. 2016, 138, 11762–11774

integrals. In **L5**, the oscillator strength is more evenly distributed across both main absorption bands, suggesting stronger $k$ = 0 FE/CTE mixing than in **L1**. Additionally, the asymmetry suggests that, for both **L1** and **L5**, the CT states lie below the vibronic FE that carries the majority of the oscillator strength. The large $k$ = 0 FE/CTE mixing in **L1** and **L5** suggests that both systems are able to generate electrons and deliver them to the catalyst. However, **L5** is expected to provide electrons to the catalyst at a faster rate due to stronger $k$ = 0 FE/CTE mixing. We test this hypothesis below by modeling both **L1** and **L5** and calculating the relative rates of charge generation.

In order to model the two PMI systems, we begin by extracting the single-molecule parameters needed to define the Hamiltonian in eq 1 from the solution spectrum (Figure 8).

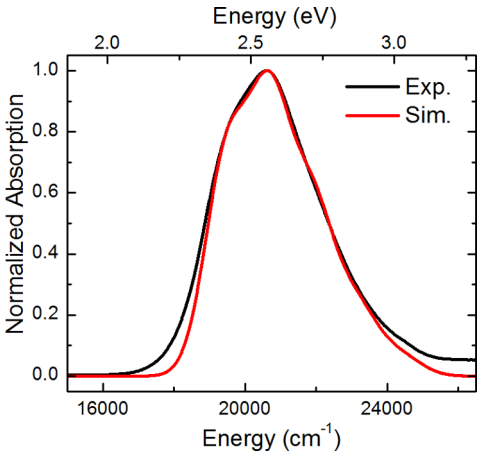


**Figure 8.** Experimental (black) and simulated (red) solution spectra of the PMIs.

The spectrum exhibits subtle vibronic features that allow for assignment of both the neutral HR factor ($\lambda_0^2$ = 1.15) and vibrational energy ($\omega_{vib}$ = 1225 cm$^{-1}$). These values are consistent with those found in other similar rylene systems.[12,22] From the solution spectrum we also obtain the absorption line width ($\sigma$ = 600 cm$^{-1}$), which is taken to be the standard deviation in a normalized Gaussian line shape function, and the transition frequency of the absorption origin ($-U - E_g$ = 19 475 cm$^{-1}$). Figure 8 shows good agreement between the simulated and measured spectra (see the SI for absorption calculation details), thereby validating the parameter set. We note that in all calculations we have used a single effective vibrational mode to account for the vibronic progression, although in reality several closely spaced modes contribute.

The PMI assemblies are modeled as one-dimensional $\pi$-stacks composed of 50 molecules (Figure 9). Due to computational considerations, we have neglected the second dimension of the PMI nanoribbon in order to focus on the charge-transfer interactions between neighboring $\pi$-stacked molecules. The charge-transfer interactions along the second dimension are expected to be weak due to the small overlap between neighboring frontier molecular orbitals. Furthermore, in order to be consistent with the phase conventions developed in sections II–IV, we have chosen the phases of the local electronic excited states so that the transition dipole moments are all aligned in the $k$ = 0 exciton.

Following the method outlined in ref 12, the vibronic coupling parameters for the ionic states were evaluated using density functional theory (DFT). The values $\lambda_+^2$ = 0.19 and $\lambda_-^2$ = 0.24 were arrived at by summing the individual HR factors of each calculated vibrational mode within 200 cm$^{-1}$ of the effective mode frequency extracted from the solution spectrum, i.e., within the range 1025–1425 cm$^{-1}$. These calculations employed the B3LYP functional and cc-pVDZ basis set and were based on DFT-optimized geometries of the PMI core with the linker group replaced by a hydrogen atom. Vibrational overlap factors were then computed on the basis of the calculated Huang–Rhys factors as in eqs 32–34 of ref 12.

The usual approach to parametrize the intermolecular interactions within crystalline systems[12−14,22] involves ab-inito calculations of the intermolecular interactions based on the crystal structure. Because the PMI nanostructures are two-dimensional ribbons there is no crystallographic information available about the dimension normal to the ribbon surface. As such, we have no experimental information about the long-axis offset in the stacking between molecules. Given the crystallinity of the material, we expect this long-axis stacking to be consistent across the material. In lieu of the usual procedure, we parametrize the intermolecular interactions based on the spectral signatures outlined in section III.

From the crystal absorption spectra (Figure 1c), we extract the magnitude of $|t_e + t_h|$ for both **L1** and **L5** from the absorption bandwidth ($\approx 4|t_e + t_h|$). In both **L1** and **L5**, the bandwidth is approximately 5000 cm$^{-1}$, resulting in a value of 1250 cm$^{-1}$ (0.16 eV) for $|t_e + t_h|$. While it is generally possible to calculate the individual CT integrals using quantum chemical software, a lack of information concerning the precise 3D

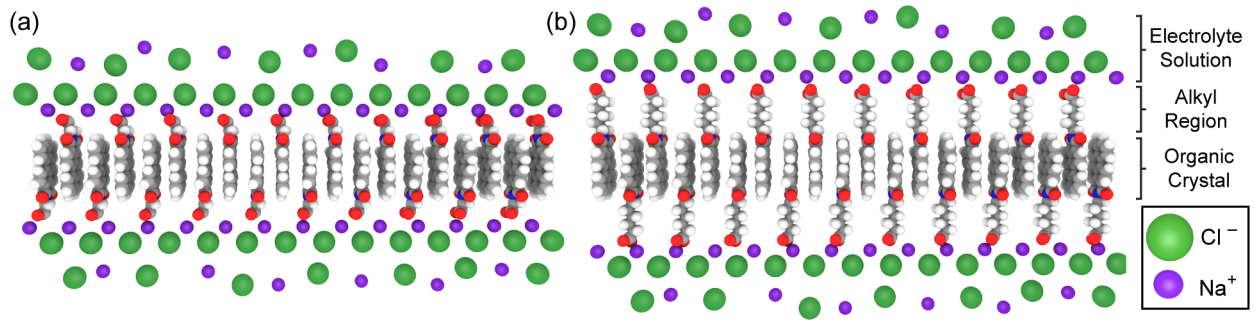


**Figure 9.** Schematic representations of 1D stacks of PMI molecules for (a) **L1** and (b) **L5** shown as cross sections of the larger, 2D assemblies. Each assembly is composed of an inner light-absorbing organic crystal and a shell of alkyl groups and is surrounded by an electrolyte solution. Water molecules are omitted for clarity. The electrolyte solution is accounted for in the model through modulation of the Coulomb potential between electron and hole.



DOI: 10.1021/jacs.6b05673
J. Am. Chem. Soc. 2016, 138, 11762–11774

packing arrangement within these systems prohibits such calculations. Therefore, we simply set $t_e = t_h$, so that the magnitude of the individual CT integrals is taken to be 625 $cm^{-1}$ (0.08 eV). We thus assume a similar $\pi$-stacking geometry for **L1** and **L5**. The assumption $t_e = t_h$ is not rigorous; however, the simulated spectrum is relatively insensitive to asymmetries in the CT integrals so long as $|t_e + t_h|$ remains constant (see the SI). These integrals are of magnitude comparable to those calculated on the basis of known $\pi$-stacked rylene crystal geometries[12,22] and are also consistent with experimental measurements of the valence bandwidths in perylene-based crystals.[56,57]

The charged nature of both the PMI molecules and surrounding electrolyte solution suggest that the electron and hole will experience significant screening. We assume that the Coulomb binding energy for nearest-neighbor charge separation obeys the inequality $V_{CT}(1) \ll 4|t_e + t_h|$, where the right-hand side is approximately 0.65 eV for the PMI systems of interest. For simplicity, we take $V_{CT} = 0$ as in sections III and IV. We further set the value of $U$ to 0.2 eV, although higher values up to 0.5 eV were also explored. Since the important mixing between Frenkel and CT states is dependent mostly on the quantity $J_{k=0} - U$, the higher values of $U$ yielded similar absorption spectra as long as $J_{k=0}$ was increased to maintain the value of $J_{k=0} - U$. In the calculated spectra of Figure 10, the

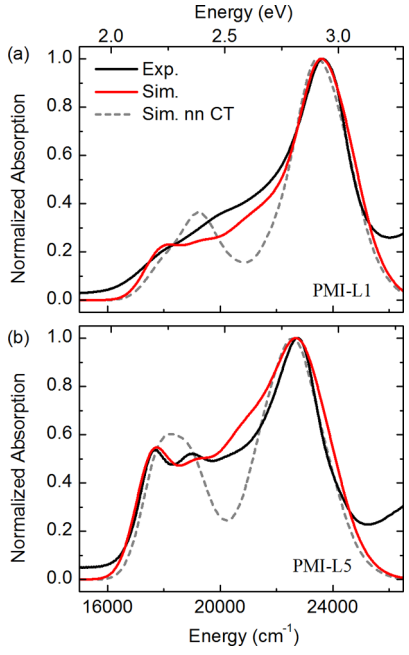


**Figure 10.** Simulated (red) spectra of (a) **L1** and (b) **L5** are compared to experiment (black). Also shown are simulations when only nearest-neighbor CT states are included (gray dash). Note that a spectral shift of $\Delta = -800$ and $-1100$ $cm^{-1}$ has been added to the simulated **L1** and **L5** spectra in order to align the most intense peak with experiment.

value of $J_{k=0}$ was adjusted to reproduce the relative intensities of the two absorption bands observed experimentally. Note again that the 2D nature of these materials limits our ability to experimentally determine the packing offset along the long molecular axis so that $J_k$ can only be approximately evaluated (see below). However, $J_{k=0}$ can be set empirically based on the absorption signatures outlined in section III. Accordingly, we used the values $J_{k=0}$ = 2200 and 1200 $cm^{-1}$ for **L1** and **L5**, respectively. (For comparison, the values increased to approximately 3400 and 2500 $cm^{-1}$ when $U$ was set to 0.4 eV.) The excitonic couplings were incorporated through the nearest neighbor interaction, which was set to $J_c = J_{k=0}/2$. Interestingly, the values for $J_{k=0}$ are less than those of infinite 2D sheets of **L1** (3850 $cm^{-1}$) and **L5** (3500 $cm^{-1}$) as calculated using transition charge densities where an approximate two-dimensional geometry, consistent with wide-angle X-ray scattering (WAXS) measurements (see SI for calculation details), was considered in the lattice sum for $J_{k=0}$. The values of $J_{k=0}$ used in the simulations are therefore consistent with *finite* nanoribbon dimensions. The larger excitonic coupling for **L1** is supported by two experimental observations. First, the WAXS data show that the intermolecular edge-to-edge spacing in **L1** is nearly 1 Å closer than for **L5**. Second, cryo-TEM measurements indicate that **L1** forms wider nanoribbon sheets than **L5**: in going from **L1** to **L5** the nanoribbon width decreases from micrometers to tens of nanometers. Both the closer spacing and wider ribbon dimensions serve to increase the magnitude of the excitonic coupling in **L1**. The entire parameter sets are summarized in Table 1.

**Table 1. Simulation Parameters for Absorption Calculations**

| parameter[a] | L1 | L5 |
|---|---|---|
| $J_{k=0}$ | 2200 | 1200 |
| $t_e$ | 625 | 625 |
| $t_h$ | 625 | 625 |
| $U$ | 1600 | 1600 |
| $V_{CT}(s)$ | 0 | 0 |
| $\omega_{vib}$ | 1225 | 1225 |
| $\lambda_0^2$ | 1.15 | 1.15 |
| $\lambda_-^2$ | 0.24 | 0.24 |
| $\lambda_+^2$ | 0.19 | 0.19 |
| $\omega_{0-0}$ | 19475 | 19475 |
| $\Delta$ | −800 | −1100 |
| $\sigma$ | 600 | 600 |

[a]All energies are expressed in units of $cm^{-1}$.

We note that for **L1**, $J_{k=0} - U > 0$, but for **L5**, $J_{k=0} - U < 0$, suggesting that the simulated absorption spectrum for **L1** should be skewed to the blue, while that of **L5** should be skewed to the red on the basis of the discussion in section III. Instead, in both cases, the simulated spectra are skewed to the blue. This unexpected behavior is a result of vibronic coupling, which redistributes oscillator strength to higher-energy vibrationally excited FEs. In any case, the quantity $|J_{k=0} - U|$ is less in **L5** compared to **L1**, which results in a much more even distribution of oscillator strength across both bands in the **L5** spectrum. The good agreement of the simulations with experiment (see Figure 10) validates the parameter sets and gives us confidence that the model accurately captures the essential photophysical properties of each system. As such, these parameter sets will provide the basis for our subsequent investigation concerning the photosensitizing ability of each chromophore.

Figure 10 also shows simulations where the CT states have been restricted to nearest neighbors (gray dashed line), in order to emphasize the importance of extended CT states for these PMI systems. When the extended CT states are neglected, the spectra develop two distinct bands with a significant drop in the intensity between the two bands. The latter effect arises because the FE is no longer able to strongly couple to the entire band of


DOI: 10.1021/jacs.6b05673
J. Am. Chem. Soc. 2016, 138, 11762−11774

CT states. Hence, including extended CT states and making them energetically accessible to the FE [i.e., $V_{CT}(1) \ll 4|t_e + t_h|$] are necessary to correctly describe these systems.

We are now poised to make predictions regarding the relative $H_2$ production between **L1** and **L5** based on the ability of these systems to provide electrons to the catalytic sites. It was previously hypothesized that the difference in $H_2$ production between the two systems originates from the relative ability of the exciton to split and form the free charges necessary to participate in the electron transfer reactions required for $H_2$ production.[10] In section IV, it was shown that optically allowed excitons will separate quickly when there is strong mixing between the $k = 0$ FE and CT states. This requires both large, in-phase CT integrals as well as near-resonant conditions for the $k = 0$ FE and CT states, so that $|t_e + t_h| \gg |J_{k=0} - U|$. On the basis of our model parameters, we know that although the CT integrals are similar for both **L1** and **L5**, the energy difference between the FE and CT states is larger in **L1** ($|J_{k=0} - U| = 600$ cm$^{-1}$) than in **L5** ($|J_{k=0} - U| = 400$ cm$^{-1}$) due to the larger excitonic coupling in **L1**. This leads to less efficient mixing between the FE and CT states in **L1**, which suppresses the ability of the exciton to split into free charges. Beyond decreasing the strength of FE/CTE mixing, the increased excitonic coupling in **L1** also leads to a blue-shifted absorption spectrum, which results in less overlap between the incident photon spectrum of the light source used for the $H_2$ production measurements (see Figure 10a) and the **L1** absorption spectrum. Hence, the difference in measured $H_2$ production between **L1** and **L5** can be largely attributed to differences in excitonic coupling, which leads to weaker $k = 0$ FE/CTE mixing and less efficient spectral overlap with the excitation lamp in **L1** compared to **L5**.

To test this hypothesis, we formulated an observable that takes into account both the FE/CTE mixing and the spectral overlap with the light source to measure the probability that the system will form a CT state after the absorption event. The more likely the system is to form a CT state, the more likely the free electron to proceed to the site of the bound catalyst for electron transfer. By defining the distribution of the incident radiation as $\Phi(\omega)$ and assuming coherent evolution after light absorption, the probability that the system will be found in a CT state after the absorption event is proportional to

$$P_{CT} \propto \int_{-\infty}^{\infty} d\omega\, Q(\omega) = \int_{-\infty}^{\infty} d\omega\, \Phi(\omega) \sum_i f_i g_i \Gamma(\omega - \omega_i) \tag{16}$$

Here, $Q(\omega)$ is equal to the product of the absorption spectrum of the incident radiation, $\Phi(\omega)$, and the PMI absorption spectrum weighted by the CT component of the absorbing eigenstates

$$g_i = \langle \Psi_i | \sum_{n,s\neq 0} c_n^\dagger c_n d_{n+s}^\dagger d_{n+s} | \Psi_i \rangle \tag{17}$$

The term $f_i$ represents the line strength for the transition from the ground state to the $i$th excited state (see the SI for details) and $\Gamma(\omega)$ is a Gaussian line shape function. Figure 11 shows $Q(\omega)$ for both **L1** and **L5** under broadband illumination (Figure 11a) and lamp illumination (Figure 11b). Taking the integral over all frequencies, the ratio $P_{CT}^{L5}/P_{CT}^{L1} = 1.8$ shows that under lamp illumination CT states form more readily in **L5** than **L1**. Hence, **L5** should deliver approximately 1.8 times more electrons to the reducing catalyst than **L1** over a constant period of time, implying a similar relative rate of $H_2$ production. This ratio is in good agreement with the experimentally measured ratio of $H_2$ production between the two systems ($2.4 \pm 0.5$).[10]

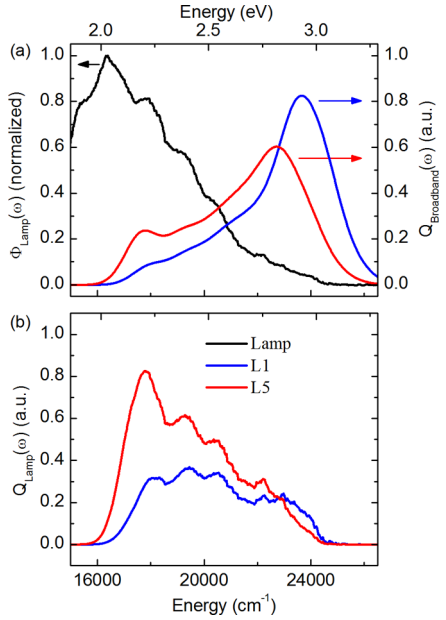


**Figure 11.** (a) The lamp spectrum used to irradiate samples in the $H_2$ photocatalysis measurements (black) and $Q(\omega)$ for **L1** and **L5** assuming broadband radiation; i.e., $\Phi(\omega)$ is constant. (b) $Q(\omega)$ for **L1** and **L5** when $\Phi(\omega)$ is given by the lamp spectrum.

## VI. DISCUSSION AND CONCLUSION

Motivated by recently developed photocatalytic systems based on self-assembling PMI amphiphiles, we investigated theoretically the absorption spectral signatures of FE/CTE mixing in systems with high dielectric constants and, therefore, weak exciton binding energies. For systems having $|t_e + t_h| > \omega_{vib}$, these signatures include (1) the asymmetry of the absorption line shape, (2) the peak splitting between the red- and blue-shifted absorption bands, and (3) the absorption intensity in the spectral region between the two bands, each of which provides complementary information about the system properties.

The asymmetry of the absorption line shape is indicative of the relative energies of the diabatic FE and CTE bands; when the absorption spectrum is skewed to the red, the $k = 0$ FE lies below the $k = 0$ CTE band, while the opposite is true when the absorption spectrum is skewed to the blue (see Figure 4). Furthermore, the peak splitting between the absorption bands is given by $\sim 4|t_e + t_h|$, providing a means of determining $|t_e + t_h|$ even in the presence of vibronic coupling. Finally, the intensity of the absorption spectrum in the spectral region midway between the two absorption bands gives information about the extent to which an FE dissociates into free charges (see Figure 5). When there is significant intensity in the interband region, extended CT states are energetically accessible to the parent FE and the exciton is able to readily dissociate into distant charges. These signatures remain valid when vibronic coupling is introduced (see Figure 4b), though it is possible for some complications to arise concerning the asymmetry of the absorption line shape depending upon the strength of the


DOI: 10.1021/jacs.6b05673
J. Am. Chem. Soc. 2016, 138, 11762−11774

vibronic coupling ($\lambda_0^2$). For example, when $\lambda_0^2 > 1$, as is the case for **L1** and **L5**, the majority of oscillator strength resides in higher vibronic states with one or more vibrational quanta. This results in the possibility of spectra that are skewed to the blue, even though $J_{k=0} - U < 0$ (as is the case in **L5**), due to the majority of oscillator strength residing with vibrationally excited FEs.

The appearance of these spectral signatures is strongly dependent on the relative phases of the CT integrals, $t_e$ and $t_e$, which depend on the molecular packing arrangement. Coupling between the CT states and the optically allowed FE depends on the sum $|t_e + t_h|$, in agreement with previous works.[12,13,20−25,33] Importantly, this sum also determines the coupling between CT states of different electron/hole radii (see eq 7) and thus the $k = 0$ CT bandwidth (see Figure 6a−c).[33] Hence, the relative phases of the CT integrals determine not only the probability of the excitation existing in a charge-separated state after absorption but also the extent to which the electron and hole are separated in such states. For applications in which efficient charge separation is desirable, it is beneficial to optimize materials to have large, in phase, CT integrals in order to maximize $|t_e + t_h|$. Indeed, Kazmaier and Hoffman observed[31] a positive correlation between the absorption width and the photogeneration of free charges in several pigment families, including perylene, squaraine,[58] thiopyrylium,[59] and diketopyrrole[60] dyes. A similar correlation between the absorption width and photocurrent generation was observed in the experiments of Gregg on perylene bis(phenethylimide),[61] Jeon et al. on titanyl phthalocyanine,[62] and Kim et al. on a series of three perylene tetracarboxylic diimide derivitives.[63] Similarly, Zhang et al. showed that an asymmetric perylene diimide characterized by a large photoconductivity also exhibits a broad absorption spectrum.[64] The other main factor influencing the FE/CTE mixing is the relative energy of the diabatic FE and CTE states. The energies of the diabatic FE states are determined mainly by the Coulomb coupling, whereas the energies of the diabatic CTE states depend on the CT integrals, as well as the dielectric environment and crystal polarizability.

Both PMI assemblies investigated in section V exhibit absorption spectral profiles consisting of two main bands with significant intensity in the spectral region lying in between. These characteristics indicate significant $k = 0$ FE/CTE mixing involving states with extended charge separation, ideal for efficient photosensitizing materials in photocatalytic applications. Instead of tightly bound excitons typically found in conventional organic materials, the excitons in these water-dispersed organic crystals readily dissociate to produce free electrons that can proceed to the catalytic reaction sites to take part in $H^+$ reduction reactions. This spontaneous charge separation allows the system to circumvent the high Coulombic barrier that typically inhibits electron transfer. This insight suggests that the formation of ordered organic materials in high dielectric environments can be greatly beneficial to producing efficient photoconversion systems.

Our calculations concerning the relative rate of $H_2$ production in **L1** and **L5** agree well with the experimentally observed $H_2$ production rates. The disparity in $H_2$ production between the systems is attributed to a difference in the ability of the materials to generate and deliver electrons to the reductive catalytic sites. On the basis of the hypothesis that the rate of charge generation within the PMI assemblies is directly correlated to the amount of $H_2$ produced, our calculations estimate that systems sensitized with **L5** should produce roughly twice as much $H_2$ as those sensitized with **L1**, in good agreement with experimental measurements. The difference in charge generation is attributed to the excitonic coupling term ($J_{k=0}$), which is significantly larger in **L1** than in **L5**, presumably due to closer edge-to-edge stacking distances and a larger nanoribbon width. This increase in $J_{k=0}$ serves to reduce the FE/CTE mixing in **L1** and is also responsible for a significant blue shift in the absorption spectrum when compared to that of **L5**. The blue shift results in less overlap of the excitation profile used for $H_2$ production experiments and **L1** absorption spectrum (see Figure 10). Together, these properties hinder exciton dissociation in **L1** compared to **L5**.

Given the inherent sensitivity of molecular coupling to structural packing in these PMI materials, there likely exists a rich electronic phase space that can be accessed through modifications in molecular design. We therefore predict the existence of crystalline PMI materials with near-zero $M$ values that when screened by a high dielectric medium should have the charge separation capacity akin to inorganic semiconductors. While the theory developed here has been applied to the photosensitizing agent in photocatalytic systems, it is not restricted to such systems or applications. For instance, in the field of singlet fission,[39,65] the CT state is thought to play an important role in mediating the conversion of a singlet exciton to a pair of triplet excitons.[66−69] The singlet and triplet pair states indirectly couple through a nearest-neighbor CT state. Such mixing should be evident as distinct signatures in the absorption and emission spectra, thereby allowing efficient screening protocols for materials with high fission rates. Overall, the theoretical approach developed here should provide guidance for developing future generations of organic electronic devices.

## ■ ASSOCIATED CONTENT

### Supporting Information

The Supporting Information is available free of charge on the ACS Publications website at DOI: 10.1021/jacs.6b05673.

Details of the multiparticle basis set, absorption calculation, Coulomb coupling lattice sums for infinite sheets of **L1** and **L5**; an illustration of the Coulomb binding well for CTEs; and ab initio calculations of the CT integrals with a discussion of the importance of the relative magnitude of $t_e$ and $t_h$. (PDF)

## ■ AUTHOR INFORMATION


### Corresponding Authors

*s-stupp@northwestern.edu
*spano@temple.edu


### Notes

The authors declare no competing financial interest.

## ■ ACKNOWLEDGMENTS

F.C.S. is supported by the National Science Foundation, Grant No. DMR-1505437. Experimental work conducted at Northwestern was supported as part of the Argonne-Northwestern Solar Energy Research (ANSER) Center, an Energy Frontier Research Center funded by the U.S. Department of Energy, Office of Science, Office of Basic Energy Sciences, under Award No. DE-SC0001059.



DOI: 10.1021/jacs.6b05673
J. Am. Chem. Soc. 2016, 138, 11762−11774

## REFERENCES


(1) Umena, Y.; Kawakami, K.; Shen, J.-R.; Kamiya, N. *Nature* **2011**, *473*, 55.
(2) Roszak, A. W.; Howard, T. D.; Southall, J.; Gardiner, A. T.; Law, C. J.; Isaacs, N. W.; Cogdell, R. J. *Science* **2003**, *302*, 1969.
(3) Scholes, G. D.; Fleming, G. R.; Olaya-Castro, A.; van Grondelle, R. *Nat. Chem.* **2011**, *3*, 763.
(4) Krieg, E.; Bastings, M. M. C.; Besenius, P.; Rybtchinski, B. *Chem. Rev.* **2016**, *116*, 2414.
(5) Haedler, A. T.; Kreger, K.; Issac, A.; Wittmann, B.; Kivala, M.; Hammer, N.; Kohler, J.; Schmidt, H.-W.; Hildner, R. *Nature* **2015**, *523*, 196.
(6) Han, Z.; Shen, L.; Brennessel, W. W.; Holland, P. L.; Eisenberg, R. *J. Am. Chem. Soc.* **2013**, *135*, 14659.
(7) Sabatini, R. P.; Eckenhoff, W. T.; Orchard, A.; Liwosz, K. R.; Detty, M. R.; Watson, D. F.; McCamant, D. W.; Eisenberg, R. *J. Am. Chem. Soc.* **2014**, *136*, 7740.
(8) McLaughlin, M. P.; McCormick, T. M.; Eisenberg, R.; Holland, P. L. *Chem. Commun.* **2011**, *47*, 7989.
(9) Weingarten, A. S.; Kazantsev, R. V.; Palmer, L. C.; McClendon, M.; Koltonow, A. R.; Samuel, A. P.; Kiebala, D. J.; Wasielewski, M. R.; Stupp, S. I. *Nat. Chem.* **2014**, *6*, 964.
(10) Weingarten, A. S.; Kazantsev, R. V.; Palmer, L. C.; Fairfield, D. J.; Koltonow, A. R.; Stupp, S. I. *J. Am. Chem. Soc.* **2015**, *137*, 15241.
(11) Hartnett, P. E.; Timalsina, A.; Matte, H. S. S. R.; Zhou, N.; Guo, X.; Zhao, W.; Facchetti, A.; Chang, R. P. H.; Hersam, M. C.; Wasielewski, M. R.; Marks, T. J. *J. Am. Chem. Soc.* **2014**, *136*, 16345.
(12) Gisslen, L.; Scholz, R. *Phys. Rev. B: Condens. Matter Mater. Phys.* **2009**, *80*, 115309.
(13) Gisslen, L.; Scholz, R. *Phys. Rev. B: Condens. Matter Mater. Phys.* **2011**, *83*, 155311.
(14) Hestand, N. J.; Yamagata, H.; Xu, B. L.; Sun, D. Z.; Zhong, Y.; Harutyunyan, A. R.; Chen, G. G.; Dai, H. L.; Rao, Y.; Spano, F. C. *J. Phys. Chem. C* **2015**, *119*, 22137.
(15) Yamagata, H.; Norton, J.; Hontz, E.; Olivier, Y.; Beljonne, D.; Bredas, J. L.; Silbey, R. J.; Spano, F. C. *J. Chem. Phys.* **2011**, *134*, 204703.
(16) Cudazzo, P.; Gatti, M.; Rubio, A. *Phys. Rev. B* **2012**, *86*, 195307.
(17) Petelenz, B.; Petelenz, P.; Shurvell, H. F.; Smith, V. H., Jr *Chem. Phys.* **1988**, *119*, 25.
(18) Tiago, M. L.; Northrup, J. E.; Louie, S. G. *Phys. Rev. B: Condens. Matter Mater. Phys.* **2003**, *67*, 115212.
(19) Roth, F.; Schuster, R.; Konig, A.; Knupfer, M.; Berger, H. *J. Chem. Phys.* **2012**, *136*, 204708.
(20) Hoffmann, M.; Soos, Z. G. *Phys. Rev. B: Condens. Matter Mater. Phys.* **2002**, *66*, 024305.
(21) Heinemeyer, U.; Scholz, R.; Gisslen, L.; Alonso, M. I.; Osso, J. O.; Garriga, M.; Hinderhofer, A.; Kytka, M.; Kowarik, S.; Gerlach, A.; Schreiber, F. *Phys. Rev. B: Condens. Matter Mater. Phys.* **2008**, *78*, 085210.
(22) Yamagata, H.; Maxwell, D. S.; Fan, J.; Kittilstved, K. R.; Briseno, A. L.; Barnes, M. D.; Spano, F. C. *J. Phys. Chem. C* **2014**, *118*, 28842.
(23) Hestand, N. J.; Spano, F. C. *J. Chem. Phys.* **2015**, *143*, 244707.
(24) Hennessy, M. H.; Soos, Z. G.; Pascal, R. A.; Girlando, A. *Chem. Phys.* **1999**, *245*, 199.
(25) Hoffmann, M.; Schmidt, K.; Fritz, T.; Hasche, T.; Agranovich, V. M.; Leo, K. *Chem. Phys.* **2000**, *258*, 73.
(26) Lim, J. M.; Kim, P.; Yoon, M. C.; Sung, J.; Dehm, V.; Chen, Z. J.; Wurthner, F.; Kim, D. *Chem. Sci.* **2013**, *4*, 388.
(27) Giaimo, J. M.; Lockard, J. V.; Sinks, L. E.; Scott, A. M.; Wilson, T. M.; Wasielewski, M. R. *J. Phys. Chem. A* **2008**, *112*, 2322.
(28) Neuteboom, E. E.; Meskers, S. C.; Meijer, E.; Janssen, R. A. *Macromol. Chem. Phys.* **2004**, *205*, 217.
(29) Hestand, N. J.; Zheng, C. Y.; Penmetcha, A. R.; Cona, B.; Cody, J. A.; Spano, F. C.; Collison, C. J. *J. Phys. Chem. C* **2015**, *119*, 18964.
(30) Delgado, M. C. R.; Kim, E.-G.; Filho, D. t. A. d. S.; Bredas, J.-L. *J. Am. Chem. Soc.* **2010**, *132*, 3375.
(31) Kazmaier, P. M.; Hoffmann, R. *J. Am. Chem. Soc.* **1994**, *116*, 9684.
(32) Hestand, N. J.; Tempelaar, R.; Knoester, J.; Jansen, T. L.; Spano, F. C. *Phys. Rev. B: Condens. Matter Mater. Phys.* **2015**, *91*, 195315.
(33) Merrifield, R. E. *J. Chem. Phys.* **1961**, *34*, 1835.
(34) Yamagata, H.; Pochas, C. M.; Spano, F. C. *J. Phys. Chem. B* **2012**, *116*, 14494.
(35) Tempelaar, R.; Koster, L. J.; Havenith, R. W.; Knoester, J.; Jansen, T. L. *J. Phys. Chem. Lett.* **2016**, *7*, 198.
(36) Förster, T. *Ann. Phys.* **1948**, *437*, 55.
(37) Scholes, G. D. *Annu. Rev. Phys. Chem.* **2003**, *54*, 57.
(38) May, V.; Kühn, O. *Charge and Energy Transfer Dynamics in Molecular Systems*; John Wiley & Sons, 2008.
(39) Smith, M. B.; Michl, J. *Chem. Rev.* **2010**, *110*, 6891.
(40) Philpott, M. R. *J. Chem. Phys.* **1971**, *55*, 2039.
(41) Spano, F. C. *J. Chem. Phys.* **2002**, *116*, 5877.
(42) Stradomska, A.; Petelenz, P. *J. Chem. Phys.* **2009**, *131*, 044507.
(43) Yamagata, H.; Spano, F. C. *J. Chem. Phys.* **2011**, *135*, 054906.
(44) Klebe, G.; Graser, F.; Hädicke, E.; Berndt, J. *Acta Crystallogr., Sect. B: Struct. Sci.* **1989**, *45*, 69.
(45) Graser, F.; Hädicke, E. *Liebigs Ann. Chem.* **1980**, *1980*, 1994.
(46) Graser, F.; Hädike, E. *Liebigs Ann. Chem.* **1984**, *1984*, 483.
(47) Buncel, E.; Mckerrow, A. J.; Kazmaier, P. M. *J. Chem. Soc., Chem. Commun.* **1992**, 1242.
(48) Yagai, S.; Seki, T.; Karatsu, T.; Kitamura, A.; Würthner, F. *Angew. Chem., Int. Ed.* **2008**, *47*, 3367.
(49) Sarbu, A.; Biniek, L.; Guenet, J.-M.; Mesini, P. J.; Brinkmann, M. *J. Mater. Chem. C* **2015**, *3*, 1235.
(50) Gregg, B. A.; Kose, M. E. *Chem. Mater.* **2008**, *20*, 5235.
(51) Balakrishnan, K.; Datar, A.; Naddo, T.; Huang, J.; Oitker, R.; Yen, M.; Zhao, J.; Zang, L. *J. Am. Chem. Soc.* **2006**, *128*, 7390.
(52) Jones, B. A.; Facchetti, A.; Wasielewski, M. R.; Marks, T. J. *J. Am. Chem. Soc.* **2007**, *129*, 15259.
(53) Wurthner, F. *Chem. Commun.* **2004**, 1564.
(54) Wurthner, F.; Kaiser, T. E.; Saha-Moller, C. R. *Angew. Chem., Int. Ed.* **2011**, *50*, 3376.
(55) These molecules were chosen as representatives from a larger set of PMI systems with various linker lengths (**L1**−**L5**, **L7**). The subset **L1**−**L4** is characterized by a similar packing arrangement, while **L5** and **L7** are characterized by a separate packing arrangement. **L1** and **L5** were chosen because there is no evidence of a probable amorphous phase in the absorption spectra as there is in the spectra of some of the other compounds (e.g., **L3** and **L4**). See ref 10.
(56) Yamane, H.; Kera, S.; Okudaira, K. K.; Yoshimura, D.; Seki, K.; Ueno, N. *Phys. Rev. B* **2003**, *68*, 033102.
(57) Gavrila, G. N.; Mendez, H.; Kampen, T. U.; Zahn, D. R. T.; Vyalikh, D. V.; Braun, W. *Appl. Phys. Lett.* **2004**, *85*, 4657.
(58) Loutfy, R. O.; Hsiao, C. K.; Kazmaier, P. M. *Photogr. Sci. Eng.* **1983**, *27*, 5.
(59) Dulmage, W. J.; Light, W. A.; Marino, S. J.; Salzberg, C. D.; Smith, D. L.; Staudenmayer, W. J. *J. Appl. Phys.* **1978**, *49*, 5543.
(60) Mizuguchi, J.; Rochat, A. C. *J. Imaging Sci.* **1988**, *32*, 135.
(61) Gregg, B. A. *J. Phys. Chem.* **1996**, *100*, 852.
(62) Jeon, H. G.; Ito, Y.; Sunohara, Y.; Ichikawa, M. *Jpn. J. Appl. Phys.* **2015**, *54*, 091601.
(63) Kim, I.; Haverinen, H. M.; Wang, Z.; Madakuni, S.; Li, J.; Jabbour, G. E. *Appl. Phys. Lett.* **2009**, *95*, 023305.
(64) Zhang, Y.; Peng, C.; Ma, X.; Che, Y.; Zhao, J. *Chem. Commun.* **2015**, *51*, 15004.
(65) Smith, M. B.; Michl, J. *Annu. Rev. Phys. Chem.* **2013**, *64*, 361.
(66) Král, K. *Czech. J. Phys. B* **1972**, *22*, 566.
(67) Monahan, N.; Zhu, X.-Y. *Annu. Rev. Phys. Chem.* **2015**, *66*, 601.
(68) Beljonne, D.; Yamagata, H.; Bredas, J. L.; Spano, F. C.; Olivier, Y. *Phys. Rev. Lett.* **2013**, *110*, 22402.
(69) Greyson, E. C.; Vura-Weis, J.; Michl, J.; Ratner, M. A. *J. Phys. Chem. B* **2010**, *114*, 14168.



DOI: 10.1021/jacs.6b05673
*J. Am. Chem. Soc.* 2016, 138, 11762−11774